

A nonlinear PDE-based method for sparse deconvolution ^{*}

Yu Mao [†] Bin Dong [‡] Stanley Osher [§]

February 10, 2010

Abstract

In this paper, we introduce a new nonlinear evolution partial differential equation for sparse deconvolution problems. The proposed PDE has the form of continuity equation that arises in various research areas, e.g. fluid dynamics and optimal transportation, and thus has some interesting physical and geometric interpretations. The underlying optimization model that we consider is the standard ℓ_1 minimization with linear equality constraints, i.e. $\min_u \{\|u\|_1 : Au = f\}$ with A being an under-sampled convolution operator. We show that our PDE preserves the ℓ_1 norm while lowering the residual $\|Au - f\|_2$. More importantly the solution of the PDE becomes sparser asymptotically, which is illustrated numerically. Therefore, it can be treated as a natural and helpful plug-in to some algorithms for ℓ_1 minimization problems, e.g. Bregman iterative methods introduced for sparse reconstruction problems in [1]. Numerical experiments show great improvements in terms of both convergence speed and reconstruction quality.

1 Introduction

The sparse deconvolution problem is to estimate an unknown sparse signal which has been convolved with some known kernel function and corrupted by noise. There are many applications of sparse deconvolution, e.g. in seismology, nondestructive ultrasonic evaluation, image restoration, or intracardiac electrograms (see e.g. [2, 3, 4, 5, 6, 7, 8]).

There has been an intensive development of sparse deconvolution techniques and algorithms. Due to their simplicity, least squares methods have been used to deconvolve sparse seismic signals [9, 10]. The major drawbacks of least squares methods are their lack of robustness and the ill-posedness of the problem when the number of unknowns is less than or equal to the number of equations. Many complementary methods have been presented, such as Tikhonov regularization [11] and the total least squares method [12, 13]. Another class of complementary methods to the classical least squares method is the ℓ_1 -penalized models [14, 15], where ℓ_1 norm of the unknown signal is used as an additional regularization term, allowing us to control the sparseness of the solution.

In the recent burst of research in compressive sensing (CS) [16, 17, 18], the following ℓ_1 minimization problem (basis pursuit) is widely used (see e.g. [19, 1])

$$\min_{u \in R^n} \{\|u\|_1 : Au = f\}, \quad (1)$$

^{*}Research supported by ONR grants: N00014-08-1-1119 and N00014-07-0810 and the Department of Defense

[†]Department of Mathematics, UCLA, Los Angeles, CA 90095 (ymao29@math.ucla.edu)

[‡]Department of Mathematics, UCSD, 9500 Gilman Drive, La Jolla, CA, 92093-0112, (bdong@math.ucsd.edu)

[§]Department of Mathematics, UCLA, Los Angeles, CA 90095 (sjo@math.ucla.edu)

where $\|u\|_1 := \sum_i |u_i|$ denotes the ℓ_1 norm of u . In our paper, we shall adopt the above optimization model with A being a convolution matrix with some known continuous differentiable kernel function (e.g. the impulse response of the system or wavelet basis). When the kernel function is everywhere nonnegative and the sparse signal we want to recover is also known to be nonnegative, we can solve the constrained least squares problem $\min_u \{\|Au - f\|_2^2 : u \geq 0\}$ as suggested by [20]. However, this model does not work for general kernel functions and signals with negative entries. Hence in this paper, we will stick to the above ℓ_1 minimization model (1), although we believe our PDE can be also added to many nonnegative least squares approaches.

To solve the constrained optimization (1), standard second-order methods such as interior-point methods were introduced in [21, 22, 23]. However, these methods, although accurate, become inefficient for large scale problems. To overcome this, large scale optimization methods have recently been developed to solve (1) or its siblings [1, 24, 25, 26, 27, 28, 29, 30, 31, 32]. These methods are very popular in CS, and all of them, especially Bregman iterations introduced to CS in [1], have outstanding performance in solving CS problems, e.g. when the matrix A is taken to be a random submatrix of some orthonormal matrix, such as Fourier or DCT matrix.

For deconvolution problems however, the above mentioned methods are usually less efficient than solving CS problems. The major reason is that each column vector of a convolution matrix A is highly coherent to the nearby columns, especially the ones that are right next to it. This makes the signal much harder to deconvolve if it has two spikes that are very close to each other. Therefore, in contrast to CS problems, the spatial information of u (i.e. the variable “ x ” of $u(x)$) is no longer irrelevant for sparse deconvolution problems, which motivates us to introduce what we call a spatial motion PDE into optimization algorithms to solve problem (1).

Intuitively speaking, this PDE should spatially move spikes around such that the constraint $Au = f$ is closer to being satisfied. However, the ℓ_1 norm of the solution should not be altered during the process. We will prove in Section 3 that our motion PDE indeed satisfies these properties. Furthermore, the PDE alone tends to sparsify the solution, which, together with its other properties, makes it an effective and powerful add-on to some of the optimization algorithms for CS problems mentioned above. In this paper, we shall combine the motion PDE with Bregman iteration [1] (with the inner unconstrained problem (3) solved by FPC [30]) to enhance its performance. We note that it is also possible to combine the motion PDE with other iterative thresholding based algorithms (e.g. the linearized Bregman iterative method in [25] or the Bregmanized operator splitting method in [28]).

The rest of the paper is organized as follows. We will first recall some basics of Bregman distance and Bregman iterations in Section 2. Then in Section 3, we introduce our motion PDE and explore its physical and geometrical meaning. In Section 4, we combine our PDE with Bregman iteration and propose our new algorithm. Numerical experiments are also conducted. Finally, we draw our conclusions in Section 5.

2 Background

In this section, we briefly recall the concept of Bregman distance [33] and Bregman iterations [1].

2.1 Bregman Distance

The Bregman distance [33], based on the convex function J , between points u and v , is defined by

$$D_J^p(u, v) = J(u) - J(v) - \langle p, u - v \rangle$$

where $p \in \partial J(v)$ is an element in the subgradient of J at the point v . In general $D_J^p(u, v) \neq D_J^p(v, u)$ and the triangle inequality is not satisfied, so $D_J^p(u, v)$ is not a distance in the usual sense. However it does measure the closeness between u and v in the sense that $D_J^p(u, v) \geq 0$ and $D_J^p(u, v) \geq D_J^p(w, v)$ for all points w on the line segment connecting u and v . Moreover, if J is convex, $D_J^p(u, v) \geq 0$, if J is strictly convex $D_J^p(u, v) > 0$ for $u \neq v$ and if J is strongly convex, then there exists a constant $a > 0$ such that

$$D_J^p(u, v) \geq a\|u - v\|_2^2.$$

2.2 Bregman Iterations

To solve (1) Bregman iteration was proposed in [1]. Given $u^0 = p^0 = 0$, we define:

$$\begin{aligned} u^{k+1} &= \arg \min_{u \in \mathbb{R}^n} \left\{ \mu \|u\|_1 - \mu \|u^k\|_1 - \langle u - u^k, p^k \rangle + \frac{1}{2} \|Au - f\|_2^2 \right\} \\ p^{k+1} &= p^k - A^T(Au^{k+1} - f). \end{aligned} \quad (2)$$

This can be written as, for $J(u) = \mu \|u\|_1$,

$$u^{k+1} = \arg \min_{u \in \mathbb{R}^2} \left\{ D_J^{p^k}(u, u^k) + \frac{1}{2} \|Au - f\|_2^2 \right\}.$$

As shown in [1], see also [34, 35], the Bregman iteration (2) can be written as, for $f^0 = 0, u^0 = 0$:

$$\begin{aligned} u^{k+1} &= \arg \min_{u \in \mathbb{R}^n} \left\{ \mu \|u\|_1 + \frac{1}{2} \|Au - f^k\|_2^2 \right\} \\ f^{k+1} &= f^k + f - Au^{k+1}. \end{aligned} \quad (3)$$

At each iteration, we will solve the problem (3) via the fixed point continuation (FPC) method proposed in [30]. Other ways of solving the unconstrained problem (3) can be found in e.g. [31, 36, 37, 38, 32, 39] and the references therein. Our improvement will work with most of these solvers. Now altogether, we have the following FPC Bregman iterations solving problem (1):

$$\begin{aligned} u^{k+1, N} &\leftarrow \begin{cases} u^{k, l+\frac{1}{2}} & \leftarrow u^{k, l} - \delta A^\top (Au^{k, l} - f^k) \\ u^{k, l+1} & \leftarrow \text{shrink}(u^{k, l+\frac{1}{2}}, \mu) \end{cases} \quad (\text{FPC}) \\ f^{k+1} &= f^k + f - Au^{k+1, N}. \end{aligned} \quad (4)$$

Here “shrink” is the soft thresholding function [40] defined as

$$\text{shrink}(x, \mu) := \begin{cases} x - \mu, & \text{if } x > \mu \\ 0, & \text{if } -\mu \leq x \leq \mu \\ x + \mu, & \text{if } x < -\mu. \end{cases}$$

Notice that, if we only perform 1 iteration for the FPC in (4), i.e. $N = 1$, this gives us another algorithm, called Bregmanized operator splitting, that also solves problem (1) [28].

3 A Spatial Motion PDE

In this section, we introduce and analyze a spatial motion PDE. The main purpose of this PDE is to spatially move and properly combine spikes in a sparse signal u , such that the residual $\|Au - f\|_2$ is reduced while $\|u\|_1$ is preserved. We will also present some interesting physical and geometric interpretations of the motion PDE. Throughout this section, u is understood as a function defined on the image domain Ω , while A is a composition of an convolution operator and a spatial restriction operator with respect to a sampling region S , and A^\top is the conjugate operator of A . In other words,

$$(Au)(x) = \chi_S(x) \int_{\Omega} K(x - y)u(y)dy \quad (5)$$

where K is a differentiable convolution kernel and χ_S is the characteristic function of S . The other operators in this section should be understood as functional operators as well.

3.1 Motivation

To analyze the desired spatial motion of the signal, we start from a characteristic point of view, i.e. observing the moving trajectory of a point mass and describing its motion. Consider a simple sparse signal that consists of an isolated spike at location c :

$$u = \delta(x - c).$$

We want to find the proper spatial motion that decreases the energy $H(u) = \frac{1}{2}\|Au - f\|_2^2$. To do this, we take the partial derivative of the energy with respect to the spatial variable c and obtain

$$\frac{\partial}{\partial c}H(u) = -\nabla_x(H'(u))\Big|_{x=c} = -\nabla_x(A^\top(Au - f))\Big|_{x=c}.$$

The above identity means that if we want to minimize $H(u)$, we can spatially move the spike along the direction $\nabla_x(A^\top(Au - f))\Big|_{x=c}$. In other words, the trajectory of the moving spike that minimizes $H(u)$ can be described as $u(x, t) = \delta(x - c(t))$ where $c(t)$ satisfies

$$c'(t) = -\nabla_x(A^\top(Au - f))\Big|_{x=c(t)}.$$

Similarly, if the initial signal is a negative spike, i.e. $u = -\delta(x - c)$, then its correct direction of spatial movement should be $\frac{\partial}{\partial c}H(u) = \nabla_x(A^\top(Au - f))\Big|_{x=c}$.

Based on this observation, we can formulate a spatial motion PDE as follows:

$$u_t + \nabla_x \cdot [ua(u)] = 0 \quad (6)$$

where $a(u)$ is the velocity field of the spatial transport. As elaborated by the examples above, the spatial velocity field $a(u)$ should be defined as

$$a(u) = -\nabla_x(A^\top(Au - f)) \cdot \text{sign}(u)$$

Thus (6) can be equivalently formulated as

$$u_t = \nabla_x \cdot [u|\nabla_x(A^\top(Au - f))]. \quad (7)$$

For definiteness we attach the initial and boundary conditions to (7) and obtain the following Cauchy problem

$$\begin{cases} u_t = \nabla_x \cdot [u|\nabla_x(A^\top(Au - f))], & (x, t) \in \Omega \times (0, T] \\ u(\cdot, 0) = u_0, u|_{\partial\Omega} = 0 \end{cases} \quad (8)$$

where u_0 is a continuous initial function. (8) is the core spatial motion PDE we will discuss throughout this paper. A locally integrable function u is called a weak solution of (8) if u satisfies the boundary condition and for any C^1 test function η the following identities hold:

$$\int_{\Omega \times (0, T]} [\eta_t \cdot u - |u|\nabla_x \eta \cdot \nabla_x(A^\top(Au - f))] dx dt = 0, \quad (9)$$

$$\lim_{t \rightarrow 0^+} \int_{\Omega} \eta(x, t) u(x, t) dx = \int_{\Omega} \eta(x, 0) u_0(x) dx. \quad (10)$$

3.2 Physical and Geometric Interpretations of PDE (7)

The equation (7) has a nice physical interpretation, and is closely related to optimal transportation and nonlinear dissipative processes. To see this, we assume $u > 0$ for now and regard u as the mass density of a certain fluid. The mass conservation can be expressed as the following continuity equation for u :

$$u_t + \nabla_x \cdot [u\vec{w}] = 0 \quad (11)$$

where \vec{w} is the velocity field that describes the spatial motion of the fluid. Darcy's law [41] connects the velocity field \vec{w} with the pressure field p by

$$\vec{w} = -\nabla_x p, \quad (12)$$

and thermodynamics tells us the pressure p is determined by the potential $E(u)$:

$$p = \partial_u E(u). \quad (13)$$

For an ideal gas in a homogeneous porous medium, the potential $E(u)$ is given by the free energy $\int Cu^m$. Thus equations (11), (12) and (13) lead to the classical porous medium equation [41]. If we replace the potential $E(u)$ by our residual $H(u)$, the combination of (11), (12) and (13) turns out to be our spatial motion equation (7).

Equation (7) can also be understood as a *gradient flow* of the potential $H(u)$ under the Wasserstein metric. In [42, 43], Otto *et al.* showed that the porous medium equation is a gradient flow under the Wasserstein metric for some given potential. Our following interpretation of (7) will be in the same spirit as in [42, 43].

Wasserstein distance is widely used in optimal transportation problems, whose fundamental goal is to find the most efficient plan to transport a density function u_0 to another density function u_1 in a mass

preserving fashion. Monge’s optimal transportation problem is to find the solution to

$$\inf_{M\#u_0=u_1} \int u_0(x)|x - M(x)|^2 dx \quad (14)$$

and the corresponding optimal value is called Wasserstein distance of order 2 (see [44, 45] for the definition of “#” and more other details). The idea of optimal transportation has been applied to various problems in image and signal processing, such as image classification [46], registration [47] and segmentation [48].

As pointed out by Otto [42], the Wasserstein distance of order 2 can be understood as a geodesic distance under a certain Riemannian structure on the set of density functions. The metric tensor g on the tangent space at u is formally defined by

$$\langle s_1, s_2 \rangle_g = \int u \nabla_x \phi_1 \cdot \nabla_x \phi_2 \quad (15)$$

where s_1 and s_2 are any two infinitesimal variations of u , and $\phi_i, i = 1, 2$, are solutions of

$$s_i + \nabla_x \cdot (u \nabla_x \phi_i) = 0. \quad (16)$$

Given the metric tensor g , the set of all density functions forms a Riemannian manifold (\mathcal{M}, g) .

Now we can formally interpret the motion PDE (7) as a gradient flow of $H(u) = \frac{1}{2} \|Au - f\|_2^2$ on (\mathcal{M}, g) . Under the Riemannian structure, the corresponding gradient of energy $H(u)$ w.r.t. g , denoted by $\text{grad}_g H(u)$, is defined by the following identity

$$\langle \text{grad}_g H(u), \vec{v} \rangle_g = \partial_{\vec{v}} H(u) \quad (17)$$

for all vector field \vec{v} on (\mathcal{M}, g) , where $\partial_{\vec{v}}$ denotes the directional derivative along \vec{v} . On the other hand, from (15) and (16) we can see that $\langle s_1, s_2 \rangle_g = \int \phi_1 s_2$ where ϕ_1 solves $s_1 + \nabla_x \cdot (u \nabla_x \phi_1) = 0$. Therefore, since u solves $u_t + \nabla_x \cdot (u \nabla_x (-\partial_u H(u))) = 0$, we have

$$\langle u_t, \vec{v} \rangle_g = \int -\partial_u H(u) \cdot \vec{v} = -\partial_{\vec{v}} H(u), \forall \vec{v} \quad (18)$$

which indicates that $u_t = -\text{grad}_g H(u)$. This elegant interpretation leads to a substantial understanding of our motion PDE (7): it gives the most natural way (in the sense of optimal transport) to spatially move the signal such that the residual $H(u)$ is decreasing.

3.3 Properties

Now we come back to the general case where u is not assumed to be positive. We have the following fairly well known properties of equations that resemble (8) that explain, to some extent, why this PDE can be utilized to improve the spatial reconstruction.

Proposition 1. *If $u(x, t), (x, t) \in \Omega \times (0, T]$ is a weak solution of (8) then $H(u(x, t)) = \frac{1}{2} \|Au - f\|_2^2$ is non-increasing over time.*

Proof. We need to show that $\frac{d}{dt}H(u(x,t)) \leq 0$. Indeed,

$$\begin{aligned} \frac{d}{dt}H(u(x,t)) &= \int H'(u) \cdot u_t dx \\ &= - \int \nabla_x(A^\top(Au - f)) \cdot [|u|\nabla_x(A^\top(Au - f))]dx \\ &= - \int |u|[\nabla_x(A^\top(Au - f))]^2 dx \leq 0 \end{aligned}$$

□

Proposition 2. *If $u(x,t)$, $(x,t) \in \Omega \times (0,T]$ is continuous weak solution of (8) then $\|u\|_1$ is conserved over time.*

Proof. For simplicity, we will prove this in the 1D case, while the proof for higher dimensions is similar. For a fixed time t , suppose $I = [a,b]$ is one of the connected component of $\{u \neq 0\}$, i.e. u has constant sign within I , then we have $u(a,t) = u(b,t) = 0$, so

$$\begin{aligned} \frac{d}{dt} \int_a^b |u| dx &= \int_a^b u_t \text{sign}(u) dx \\ &= \text{sign}(u) \cdot \int_a^b \nabla_x \cdot [|u|\nabla_x(A^\top(Au - f))] \\ &= \text{sign}(u) \cdot [|u|\nabla_x(A^\top(Au - f))] \Big|_{x=a}^{x=b} = 0 \end{aligned}$$

Therefore overall we have $\frac{d}{dt}\|u\|_1 = 0$.

□

The above two propositions show that, although the total mass of u is preserved over time, the spatial mass distribution is adjusted such that the equation $Au = f$ is better satisfied.

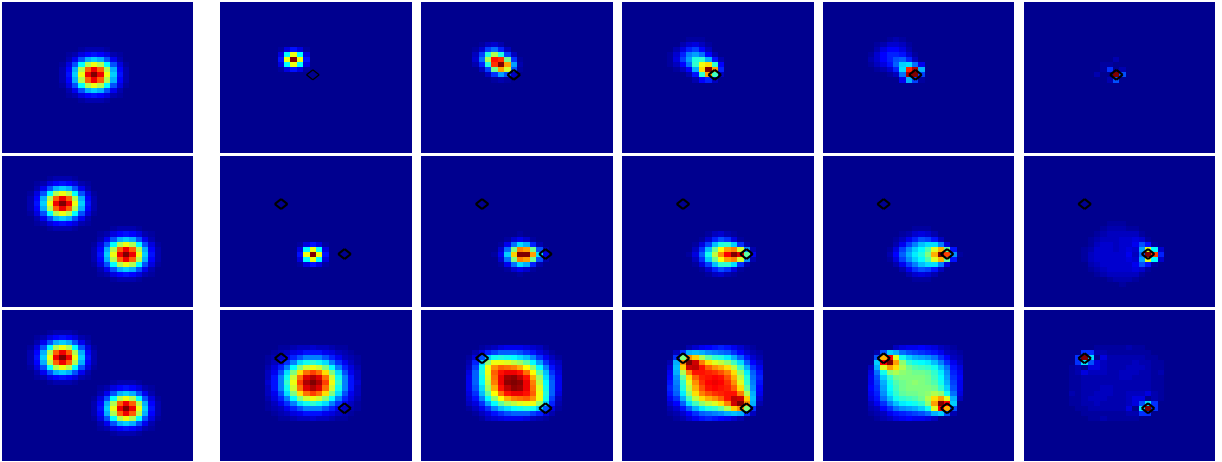


Figure 1: The first column are observed images f obtained from convolution of a Gaussian with one or two spikes. The the second column shows the initial functions u_0 and the remaining 4 columns show the corresponding solutions of spatial motion PDE (7) at time $T=250, 500, 750, 2000$ respectively. The difference between the second and third rows reflect the fact that with the same f , different choices of initial value will lead to different results.

Another and yet more important property of the motion PDE (8) is that the solution $u(x, t)$ becomes sparser asymptotically in t . We illustrate this phenomena numerically in Figure 1, where the peaks of the solution u move to the correct locations, and when they are close to the desired locations, u begins to become sparser which is desired for sparse reconstruction problems. This explains why we can get more accurate solutions when combining the motion PDE (8) with FPC Bregman iterations (see Section 4.3.2 for more details).

It is also worth noticing that, comparing the second and the third rows of Figure 1, for different initial functions u_0 , the solutions of PDE (8) have rather different asymptotic behavior. This means that the residual $H(u)$ is not convex under the Wasserstein metric. In fact, the solution in the second row of Figure 1 only approximates a local minimizer of $H(u)$ with respect to the Wasserstein metric but not a global one, i.e. $H(u) \neq 0$ in this case, but $\text{grad}_g H(u) = 0$.

4 Numerical Schemes and Experiments

4.1 Numerical Implementation of PDE (8)

The finite difference scheme that we use for our motion PDE is as follows:

$$\frac{u_{i,j}^{n+1} - u_{i,j}^n}{dt} = D_-^x \left[|u_{i+\frac{1}{2},j}^n| D_+^x p_{i,j}^n \right] + D_-^y \left[|u_{i,j+\frac{1}{2}}^n| D_+^y p_{i,j}^n \right], \quad (19)$$

where

$$\begin{aligned} D_-^x u_{i,j} &= u_{i,j} - u_{i-1,j}, & D_+^x u_{i,j} &= u_{i+1,j} - u_{i,j}, \\ D_-^y u_{i,j} &= u_{i,j} - u_{i,j-1}, & D_+^y u_{i,j} &= u_{i,j+1} - u_{i,j} \\ |u_{i+\frac{1}{2},j}^n| &:= \begin{cases} \frac{|u_{i+1,j}^n| + |u_{i,j}^n|}{2}, & u_{i+1,j} u_{i,j} > 0, \\ 0 & \text{otherwise} \end{cases} \\ |u_{i,j+\frac{1}{2}}^n| &:= \begin{cases} \frac{|u_{i,j+1}^n| + |u_{i,j}^n|}{2}, & u_{i,j+1} u_{i,j} > 0, \\ 0 & \text{otherwise} \end{cases} \end{aligned}$$

and

$$p^n = A^\top (A u^n - f)$$

where the operator A is implemented by standard matrix multiplication. The special definition of $|u_{i+\frac{1}{2},j}^n|$ and $|u_{i,j+\frac{1}{2}}^n|$ above is to make sure that the ℓ_1 norm of u^k is exactly preserved in the discrete setting.

To guarantee the stability of the numerical solution, the time step dt should be chosen appropriately. Although it is hard to derive a explicit stable condition for our nonlinear PDE, for each step we can treat the PDE as a transport equation with a fixed velocity field, and find a necessary stability condition, which is given by

$$\frac{1}{dt^n} \geq \max_{i,j} \{|D_+^x p_{i,j}^n|, |D_+^y p_{i,j}^n|\}. \quad (20)$$

4.2 Algorithm

As we explained in section 3.3, the PDE (8) does not necessarily lead to a correct solution of the optimization problem (1). However, it helps the function to be more sparse while decreasing the residual. Therefore it can

be combined with other existing deconvolution algorithm and improve the performance. Since the motion PDE (8) is time-dependent, it is natural to combine the numerical scheme (19) with FPC Bregman iteration (4) and introduce the following algorithm:

$$\begin{aligned}
u^{k+1,N} &\leftarrow \begin{cases} u^{k,l+\frac{1}{3}} &\leftarrow u^{k,l} - \delta A^\top (Au^{k,l} - f^k) \\ u^{k,l+\frac{2}{3}} &\leftarrow u^{k,l+\frac{1}{3}} + dt \nabla_x \cdot \left[|u^{k,l+\frac{1}{3}}| \nabla_x (A^\top (Au^{k,l} - f^k)) \right] \\ u^{k,l+1} &\leftarrow \text{shrink}(u^{k,l+\frac{2}{3}}, \mu) \end{cases} \quad (\text{PDE Update}) \\
f^{k+1} &= f^k + f - Au^{k+1,N}.
\end{aligned} \tag{21}$$

We shall refer to the above algorithm as PDE-FPC Bregman iterations.

We further note that for each iteration the PDE update only slightly increases the complexity, because we do not need to recalculate the term $A^\top (Au - f)$ and the finite difference operator (19) can be implemented rather efficiently.

We want to point out that this PDE update step can be similarly imposed to many other iterative thresholding based algorithms, e.g. the linearized Bregman iterative method [25] or the BOS method [28]. As far as we tested, this complementary step always improves the performance and accuracy of these algorithms without increasing the computational complexity very much. In many cases the improvement is very significant.

Remark: Note that the inner loop of (21) contains $N \geq 1$ iterations, as in the original FPC algorithm. The choice of N is not critical for the convergence of the scheme, however it affects the performance. When N is small, the algorithm converges faster (in terms of total number of iterations) while the decay of the residual is more oscillatory; when N is large, it converges slower while the decay of the residual appears more stable. In our experiments we choose $N = 10$, which seems to give us a good balance between the speed and decay of residual.

4.3 Numerical Results

In this section, we compare the performance of FPC Bregman iterations (4) with that of PDE-FPC Bregman iterations (21). We will first consider the case where there is not any noise in f , and compare the convergence speed. Then we consider a noisy case and compare the accuracy of the solutions obtained from the two algorithms. The operator A is taken to be a convolution operator with a Gaussian kernel. The clean and noisy f are shown in Figure 2, where the size of the images is 50×50 . The two kernels of the clean blurry images are generated by Matlab function `fspecial('gaussian', [41 41], σ)` with $\sigma = 4$ and 4.5 respectively. The noisy images are generated by adding Gaussian white noise to the clean blurry image with kernel `fspecial('gaussian', [21 21], 5.5)`. The intensities of the spikes are generated randomly in $[0.5, 1]$ with locations indicated by the black circles (Figure 2).

4.3.1 Convergence Speed

We consider the noise free case (left two images in Figure 2). Here we take the stopping criteria $\frac{\|u^k - \bar{u}\|_2}{\|\bar{u}\|_2} < 10^{-2}$, where \bar{u} is the true solution. The following table summaries the comparison results with various choices of parameter μ . The time step dt for the PDE is chosen to reflect best performance for given μ . From Table 1 and Table 2 we can see that PDE-FPC Bregman is generally faster than FPC Bregman in terms of computational time. Furthermore, the smaller μ gets, the more PDE-FPC Bregman outperforms FPC Bregman. The reason is that for small μ , u^k is more regular (i.e. less sparse) than for large μ due to

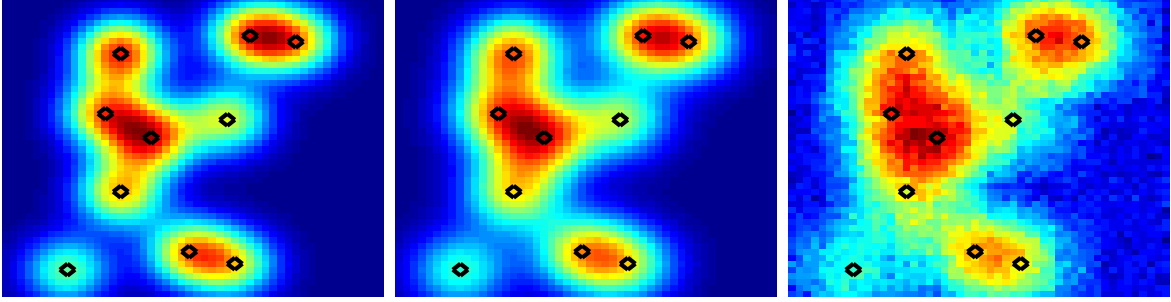


Figure 2: Clean observed images generated by different Gaussian kernels(left and middle). Noisy observed image (right) with SNR=15.87. Black circles indicating the locations of the spikes.

thresholding, and hence the PDE update in (21) will have a much nicer behavior. Also, a larger time step dt is allowed when u^k is more regular.

It is also worth noticing from Table 1 and 2 that the best performance of PDE-FPC Bregman is 6 and 10 times faster respectively than that of FPC Bregman (marked by “♠”). The more blurry is the image, the bigger is the improvement of PDE-FPC Bregman over FPC Bregman.

Table 1: Comparisons of FPC Bregman (4) and PDE-FPC Bregman (21). The symbol “♠” labels the best results for FPC Bregman and PDE-FPC Bregman.

(δ, μ)	dt	FPC Bregman		PDE-FPC Bregman	
		#Iterations	Time (sc)	#Iterations	Time (sc)
(2, 0.5)	0.2	2824	13.21	2816	14.97
(2, 0.2)	0.5	2196	10.69 ♠	1705	9.23
(2, 0.1)	2.0	2585	12.43	1324	7.06
(2, 0.05)	4.5	3365	16.04	1291	6.91
(2, 0.01)	300.0	4997	24.20	587	3.20
(2, 0.002)	800.0	9622	47.76	280	1.64
(2, 0.001)	1200.0	13386	67.73	243	1.48 ♠

4.3.2 Accuracy

We now consider the noisy case (right image in Figure 2). Experimental results are summarized in the following Table 3. Since there is noise in f , the error, which is taken to be $\frac{\|u^k - \bar{u}\|_2}{\|\bar{u}\|_2}$, generally decreases first and then increases, and u^k will eventually converge to something noisy. Therefore, in order to reflect the best performance of both algorithms, we recorded the number of iterations and computation time that correspond to the smallest error possible for each given set of parameters. From Table 3 we can see that, for each given μ , although PDE+FPC Bregman may not always be faster than FPC Bregman, it always produces a solution with a smaller error. If we consider the best set of parameters for the two algorithms, PDE-FPC Bregman outperforms FPC Bregman in terms of both computation time and accuracy.

Table 2: Comparisons of FPC Bregman (4) and PDE-FPC Bregman (21). The symbol “♠” labels the best results for FPC Bregman and PDE-FPC Bregman.

(δ, μ)	dt	FPC Bregman		PDE-FPC Bregman	
		#Iterations	Time (sc)	#Iterations	Time (sc)
(2, 0.5)	0.25	5327	25.37	4808	25.33
(2, 0.2)	0.9	4115	19.81 ♠	2904	15.26
(2, 0.1)	2.0	4651	22.13	2562	13.70
(2, 0.05)	5.0	5836	28.31	1876	10.31
(2, 0.01)	300.0	8460	41.42	1030	5.61
(2, 0.002)	1500.0	14996	74.01	446	2.53
(2, 0.001)	2000.0	22466	112.29	328	1.91 ♠

Table 3: Comparisons of FPC Bregman (4) and PDE-FPC Bregman (21). The symbol “♠” labels the best computational time and error respectively for FPC Bregman and PDE-FPC Bregman.

(δ, μ)	dt	FPC Bregman			PDE-FPC Bregman		
		#Iterations	Time (sc)	Error	#Iterations	Time (sc)	Error
(2, 0.8)	0.01	13299	17.52	1.12e-001	13417	24.61	1.04e-001
(2, 0.5)	0.05	6086	7.74	2.68e-002 ♠	6033	10.81	1.63e-002
(2, 0.2)	0.5	3663	4.61	5.70e-002	3321	5.94	2.40e-002
(2, 0.05)	1.5	2127	2.94 ♠	4.87e-002	1424	2.59	1.42e-002
(2, 0.01)	3.0	2404	3.49	5.17e-002	1651	3.09	1.47e-002
(2, 0.005)	4.0	2511	3.81	9.00e-002	1406	2.73	1.93e-002
(2, 0.002)	45.0	2985	4.92	1.87e-001	571	1.20 ♠	1.26e-002 ♠
(2, 0.001)	40.0	2730	4.70	4.05e-001	623	1.38	5.22e-002

5 Conclusions

In this paper, we introduced a new nonlinear evolution PDE for sparse deconvolution problems. We showed that this spatial motion PDE preserves the ℓ_1 norm while lowering the residual $\|Au - f\|_2$. We also showed numerically that the solution of the motion PDE tends to become sparse and converges to delta functions asymptotically. Therefore, utilizing these properties of the PDE, our proposed PDE-FPC Bregman iterations (21) outperformed the original FPC Bregman iterations [1] in terms of both convergence speed and reconstruction quality. This was strongly supported by our numerical experiments. We finally note that our PDE can also be used to enhance performance for many other iterative thresholding based algorithms, e.g. [25, 28, 39].

References

- [1] Wotao Yin, Stanley Osher, D Goldfarb, and J Darbon. Bregman iterative algorithms for l_1 -minimization with applications to compressed sensing. *SIAM J. Imaging Sci*, 1(1):143–168, 2008.
- [2] J.M. Mendel and CS Burrus. Maximum-likelihood deconvolution: a journey into model-based signal processing. 1990.

- [3] MS O'Brien, AN Sinclair, and SM Kramer. Recovery of a sparse spike time series by L norm deconvolution. *IEEE Transactions on Signal Processing*, 42(12):3353–3365, 1994.
- [4] T. Olofsson and E. Wennerstrom. Sparse deconvolution of B-scan images. *IEEE Transactions on Ultrasonics, Ferroelectrics and Frequency Control*, 54(8):1634–1641, 2007.
- [5] T. Olofsson and T. Stepinski. Maximum a posteriori deconvolution of sparse ultrasonic signals using genetic optimization. *Ultrasonics*, 37(6):423, 1999.
- [6] T. Olofsson. Semi-sparse deconvolution robust to uncertainties in the impulse responses. *Ultrasonics*, 42(1-9):969–975, 2004.
- [7] N.P. Galatsanos, A.K. Katsaggelos, R.T. Chin, and A.D. Hillery. Least squares restoration of multi-channel images. *IEEE Transactions on Signal Processing*, 39(10):2222–2236, 1991.
- [8] W.S. Ellis, S.J. Eisenberg, D.M. Auslander, M.W. Dae, A. Zakhor, and M.D. Lesh. Deconvolution: a novel signal processing approach for determining activation time from fractionated electrograms and detecting infarcted tissue. *Circulation*, 94(10):2633–2640, 1996.
- [9] AJ Berkhout. Least-squares inverse filtering and wavelet deconvolution. *Geophysics*, 42:1369, 1977.
- [10] C.L. Lawson and R.J. Hanson. *Solving least squares problems*. Society for Industrial Mathematics, 1995.
- [11] A.N. Tikhonov, V.Y. Arsenin, and F. John. *Solutions of ill-posed problems*. VH Winston Washington, DC, 1977.
- [12] G.H. Golub and C.F. Van Loan. An analysis of the total least squares problem. *SIAM Journal on Numerical Analysis*, pages 883–893, 1980.
- [13] S. Van Huffel and J. Vandewalle. The total least squares problem: computational aspects and analysis. 1991.
- [14] HL Taylor, SC Banks, and JF McCoy. Deconvolution with the l 1 norm. *Geophysics*, 44(1):39–52, 1979.
- [15] HWJ Debye and P. Riel. Lp-norm deconvolution 1. *Geophysical Prospecting*, 38(4):381–403, 1990.
- [16] Emmanuel J Candes, JK Romberg, and Terence Tao. Stable signal recovery from incomplete and inaccurate measurements. *Communications on Pure and Applied Mathematics*, 59(8), 2006.
- [17] Emmanuel J Candes, JK Romberg, and Terence Tao. Robust uncertainty principles: exact signal reconstruction from highly incomplete frequency information. *IEEE Transactions on Information Theory*, 52(2):489–509, 2006.
- [18] David L Donoho. Compressed sensing. *IEEE Transactions on Information Theory*, 52(4):1289–1306, 2006.
- [19] S.S. Chen, D.L. Donoho, and M.A. Saunders. Atomic decomposition by basis pursuit. *SIAM review*, pages 129–159, 2001.
- [20] Alfred M Bruckstein, Michael Elad, and Michael Zibulevsky. On the uniqueness of nonnegative sparse solutions to underdetermined systems of equations. *IEEE Transactions on Information Theory*, 54(11):4813–4820, 2008.

- [21] E. Candès and J. Romberg. ℓ_1 -magic. Available at www.l1-magic.org, 2007.
- [22] K. Koh, S.J. Kim, and S. Boyd. Solver for ℓ_1 -regularized least squares problems.
- [23] M. Lustig, D. Donoho, and J.M. Pauly. Sparse MRI: The application of compressed sensing for rapid MR imaging. *Magnetic Resonance in Medicine*, 58(6):1182–1195, 2007.
- [24] J. Darbon and Stanley Osher. Fast discrete optimizations for sparse approximations and deconvolutions. preprint 2007.
- [25] Stanley Osher, Y. Mao, B. Dong, and Wotao Yin. Fast linearized Bregman iteration for compressive sensing and sparse denoising. *Communications in Mathematical Sciences*, 2009. To appear.
- [26] J.F. Cai, S. Osher, and Z. Shen. Linearized Bregman iterations for compressed sensing. *Math. Comp.*, 78:1515–1536, 2009.
- [27] J. Cai, S. Osher, and Z. Shen. Convergence of the linearized Bregman iteration for ℓ_1 -norm minimization. 2008. UCLA CAM Report 08-52.
- [28] X. Zhang, M. Burger, X. Bresson, and S. Osher. Bregmanized nonlocal regularization for deconvolution and sparse reconstruction. *UCLA CAM Report*, pages 09–03, 2009.
- [29] S. Becker, J. Bobin, and E. Candes. NESTA: A Fast and Accurate First-order Method for Sparse Recovery. *Arxiv preprint arXiv:0904.3367*, 2009.
- [30] E. Hale, W. Yin, and Y. Zhang. A fixed-point continuation method for ℓ_1 -regularization with application to compressed sensing. *CAAM Technical Report TR, Rice University, Houston, TX*, pages 07–07, 2007. CAAM Technical Report TR07-07, Rice University, Houston, TX.
- [31] M.A.T. Figueiredo, R.D. Nowak, and S.J. Wright. Gradient projection for sparse reconstruction: Application to compressed sensing and other inverse problems. *IEEE Journal of Selected Topics in Signal Processing*, 1(4):586, 2007.
- [32] E. van den Berg and M.P. Friedlander. Probing the Pareto frontier for basis pursuit solutions. *SIAM Journal on Scientific Computing*, 31(2):890–912, 2008.
- [33] L.M. Bregman. The relaxation method of finding the common point of convex sets and its application to the solution of problems in convex programming. *USSR Computational Mathematics and Mathematical Physics*, 7(3):200–217, 1967.
- [34] Stanley Osher, M. Burger, D. Goldfarb, Jinjun Xu, and Wotao Yin. An iterative regularization method for total variation-based image restoration. *Multiscale Model Sim.*, 4(2):460–489, Jan 2005.
- [35] T-C. Chang, L. He, and T. Fang. Mr image reconstruction from sparse radial samples using bregman iteration. *Proceedings of the 13th Annual Meeting of ISMRM*, 2006.
- [36] S.J. Kim, K. Koh, M. Lustig, S. Boyd, and D. Gorinevsky. A method for large-scale ℓ_1 -regularized least squares problems with applications in signal processing and statistics. *Preprint*, 2007.
- [37] D.L. Donoho, Y. Tsaig, I. Drori, and J.L. Starck. Sparse solution of underdetermined linear equations by stagewise orthogonal matching pursuit. *preprint*, 2006.

- [38] Y. Nesterov. Gradient methods for minimizing composite objective function. *Center for Operations Research and Econometrics (CORE), Catholic University of Louvain, Tech. Rep*, 76:2007, 2007.
- [39] M.A.T. Figueiredo and R.D. Nowak. An EM algorithm for wavelet-based image restoration. *IEEE Transactions on Image Processing*, 12(8):906–916, 2003.
- [40] D.L. Donoho. De-noising by soft-thresholding. *IEEE transactions on information theory*, 41(3):613–627, 1995.
- [41] J.L. Vazquez. *The porous medium equation: mathematical theory*. Oxford University Press, USA, 2007.
- [42] F Otto. The geometry of dissipative evolution equations: The porous medium equation. *Commun Part Diff Eq*, 26(1-2):101–174, Jan 2001.
- [43] F Otto and M Westdickenberg. Eulerian calculus for the contraction in the Wasserstein distance. *SIAM Journal on Mathematical Analysis*, 37(4):1227–1255, Jan 2006.
- [44] C. Villani. *Topics in optimal transportation*. Amer Mathematical Society, 2003.
- [45] Cédric Villani. Optimal transportation, dissipative pde’s and functional inequalities, Jan 2003.
- [46] Y Rubner, C Tomasi, and L.J Guibas. A metric for distributions with applications to image databases. *Computer Vision, 1998. Sixth International Conference on*, pages 59–66, 1998.
- [47] S Haker, L Zhu, A Tannenbaum, and S Angenent. Optimal mass transport for registration and warping. *Int J Comput Vision*, 60(3):225–240, Jan 2004.
- [48] Kangyu Ni, Xavier Bresson, Tony F Chan, and Selim Esedoglu. Local histogram based segmentation using the Wasserstein distance. *Int J Comput Vision*, 84(1):97–111, Jan 2009.